NUMERICAL STUDY ON HEAT TRANSFER DETERIORATION OF N-DECANE DURING PYROLYSIS UNDER SUPERCRITICAL PRESSURE IN A VERTICAL TUBE

Zhiliang LEI[1, 2], Zewei BAO[3, *]

[1] College of Civil Aviation Safety Engineering, Civil Aviation Flight University of China, Deyang, Sichuan 618307, China

[2] Key Laboratory of Fire Science and Safety Engineering of Sichuan Province, Deyang, Sichuan 618307, China

[3] School of Chemical Engineering, Sichuan University, Chengdu 610065, China

[*] Corresponding author; Email: zewei.bao@scu.edu.cn

For accelerating hypersonic vehicles, it is important to understand the effects of various factors on heat transfer deterioration. The heat transfer characteristics of supercritical n-decane with pyrolysis were numerically simulated inside a vertical tube. The effects of flow direction, mass flow rate, heat flux, inlet temperature, and flight acceleration on the heat transfer characteristics were investigated. When the inlet temperature was relatively low or the fluid was decelerated vertically upward, a typical M-shaped velocity distribution was formed, indicating the heat transfer deterioration (HTD). Furthermore, the decrease in wall heat flux, as well as the increase in mass flow rate, inlet temperature and flight acceleration in the same direction as the flow makes the HTD gradually disappear. Finally, a new relationship was established between the heat flux and the flight acceleration and inlet temperature to determine critical heat flux under which HTD developed in the upward flow.

Key words*: Heat transfer deterioration; N-decane; Supercritical pressure; Pyrolysis; Vertical tube*

1. Introduction

The development of scramjet engines with high Mach numbers relies on regenerative cooling technology [1, 2]. For regenerative cooling technology, thermophysical properties of hydrocarbon fuels can drastically vary in the critical or pseudo-critical regions, risking heat transfer deterioration (HTD). HTD requires special attention when designing a regenerative cooling system because any unexpected wall temperature peak in the cooling channel reduces the efficiency and safety of the system [3-5]. Therefore, understanding the peculiarities of HTD is important to realize regenerative cooling systems with supercritical hydrocarbon fuels.

For many years, the exact mechanism of HTD in supercritical fluids has been studied. In the conventional view, HTD is resulted from radial variations in thermophysical properties, thermal acceleration, and buoyancy [6-13]. HTD phenomena of n-decane inside a horizontal circular tube was investigated and the critical conditions of HTD onset was proposed [6]. Liu *et al.* [7] reported a

numerical study on the HTD of RP-3 aviation kerosene flowing inside a vertical channel. Dang *et al.* [8] found that the HTD of RP-3 developed inside a horizontal circular channel when the wall heat flux exceeded the critical value and the wall temperature approached the pseudo-critical temperature (T_{pc}). Xu *et al.* [10] analyzed the relationship between the location at which local fluid temperature equaled T_{pc} and the turbulent boundary layer inside a vertical tube. They found that $y^+|_{T_f=T_{pc}}=5$ was where there was an onset of HTD for the upward flow. The ability of empirical formulations to determine buoyancy influences on the supercritical heat transfer of RP-3 inside horizontal tubes were analyzed [11]. They found that the modified criterion proposed by Petukhov *et al.* [12] worked well under the tested conditions [11]. Li *et al.* [13] studied HTD phenomenon of upward and downward flows of n-decane under supercritical pressure inside a circular tube. They observed an "M" type velocity profile along the radial direction and larger velocity gradients in the buffer layer, which leads to HTD.

1.1. Identification of the HTD onset

In the vast majority of studies, HTD occurs when the wall temperature peaks at one or more locations along the heated wall of the cooling channel [3, 14]. In other studies, HTD is identified when the minimum dT_w/dx is negative [15]. HTD onset has also been determined by comparing measured heat transfer coefficients with predicted values based on conventional heat transfer correlations [16]. Aside from these three common methods, Huang *et al.* [17] observed two types of HTD of aviation kerosene under supercritical pressures. Type I HTD occurs where the wall temperature (T_w) exceeds the T_{pc}, whereas Type II HTD occurs where $T_f > T_{pc}$ [17]. This paper adopts the heat transfer deterioration identification method in Ref. [15].

1.2. Correlations of the critical heat flux of HTD onset

Numerous studies [18-22] have found that HTD occurs at some critical heat flux (q_{onset}). Table 1 lists several correlations proposed for predicting q_{onset}. As evidenced in the Tab. 1, no general relationship can currently predict the HTD of all supercritical fluids. Most of these correlations specify q_{onset} as a power function of the mass flux G, namely, $q_{onset} = mG^n$ [22]. Kline *et al.* [3] suggested that not only the mass flux as well as pressure but also the tube diameter should be included in these correlations. Guo *et al.* [23] found that HTD is additionally affected by the flow direction and inlet temperature. In an upward flow, local HTD occurs only when $T_{in} < T_{pc}$ and might be alleviated by increasing T_{in} [23]. Liang *et al.* [4] showed that flight acceleration (Ac) also influenced HTD. In summary, the design parameters like pressure, tube inner diameter, inlet temperature, mass flux, and flight acceleration affect critical heat flux at which HTD appears. Among these parameters, the inlet temperature and flight acceleration have received little attention in HTD analyses. In addition, the correlation for the comprehensive influence of various factors on the critical heat flux has not been established.

Table 1. Several existing correlations for q_{onset} of supercritical fluids.

Author	Correlation	Fluid	Application range p (MPa)/G (kgm^{-2}s^{-1})/g (ms^{-2})
Yamagata *et al.* [18]	$q_{onset} = 0.2G^{1.2}$	H_2O	22.6–31/310–1830/–
Mokry *et al.* [19]	$q_{onset} = -58.97+0.745G$	H_2O	24/200–1500/–
Urbano *et al.* [15]	$q_{onset} = (0.0432p + 0.0314)G$	CH_4	13/8500/–
Zhou *et al.* [20]	$q_{onset} = 8.55\times10^{-8}(G^2 + 160Gp + 479.5322p^2 - 1894.7G + 4327.5p - 498250)$	C_5H_{12}	3–15/333.3–1666.7/–
Wang *et al.* [6]	$q_{onset} = (0.225p - 0.407)G$	$C_{10}H_{22}$	3–5/400–1200/–
Liang *et al.* [4]	$q_{onset} = (ag^3 + bg^2 + cg + d)G$	$C_{10}H_{22}$	4/–/-40–40
Kline *et al.* [3]	$q_{onset} = 0.0002G^2(0.7 + \frac{1-0.7}{1+\exp[4/(d/8-2.35)]})$	CO_2	8.35/300–1500/–

Note: $-40 \le Ac \le -1$: $a = 4.24 \times 10^{-7}$, $b = 5.83 \times 10^{-5}$, $c = 5.24 \times 10^{-3}$, $d = 6.58 \times 10^{-1}$; $0 \le Ac \le 40$: $a = 0$, $b = 0$, $c = 4.26 \times 10^{-3}$, $d = 6.69 \times 10^{-1}$.

Some aircrafts often encounter with flight acceleration, such as 2–3g for the take-off acceleration of fighter aircrafts [24]. Liang *et al.* [4] observed two types of HTD of n-decane under various flight accelerations. Lv *et al.* [24] studied the heat transfer of supercritical RP-3 inside a horizontal tube under various gravitational accelerations. They found that the onset of the HTD occurred earlier with increased gravitational acceleration increased [24]. Supercritical heat transfer of n-decane inside a horizontal channel were numerically investigated under varying acceleration states [25]. The acceleration weakened intensity of the first HTD but had little effect on its appearance location [25].

For regenerative cooling, the critical heat flux initiating HTD in hydrocarbon fuels should be predicted through correlations. However, a few existing correlations of determining critical heat flux of HTD onset do not consider the inlet temperature and flight acceleration. In addition, the effects of inlet temperature and flight acceleration on heat transfer of supercritical hydrocarbon fuels with pyrolysis are rarely studied. In this study, the effects of mass flow rate, heat flux, inlet temperature, flight acceleration, and flow direction on the thermal cracking and heat transfer of supercritical n-decane were numerically investigated inside vertical circular channel. Critical heat flux of n-decane inside the vertical upward flow tube was then predicted by a new correlation model that includes the flight acceleration and inlet temperature.

2. Simulation

2.1. Physical model and boundary conditions

Figure 1 presents the schematic diagram of a uniformly heated vertical tube. The length and inner diameter of the tube are 900 and 2 mm, respectively. A 600-mm-long heated section is fed with heat

flux varied from 0.4 to 1.2 MW/m^2. The vertical tube is modeled inside a two-dimensional axial symmetric domain.

The buoyancy effect on HTD of hydrocarbon fuels is usually conducted at gravitational acceleration of 9.8 m/s^2. However, flight acceleration *Ac* may change for a scramjet [4, 24]. To study the effect of flight acceleration on the HTD, *Ac* was varied as −29.4, −19.6, −9.8, 0.0, 9.8, 19.6, and 29.4 m/s^2. In this study, a negative flight acceleration value and a positive one indicate an upward deceleration and upward acceleration, respectively. The operating pressure was 5 MPa, and the inlet temperature and mass flow rate were 300–500 K and 2–6 g/s, respectively. All the selected geometric and operating parameters reflect the practical regenerative cooling conditions in scramjets [4, 6].

2.2. Chemical kinetics model and thermophysical property

The pyrolysis process was described by one-step PPD model [26]:

$$\begin{aligned} C_{10}H_{22} \rightarrow\ & 0.151H_2 + 0.143CH_4 + 0.256C_2H_4 + 0.126C_2H_6 + 0.230C_3H_6 \\ & + 0.180C_3H_8 + 0.196C_4H_8 + 0.102C_4H_{10} + 0.171C_5H_{10} + 0.124C_5H_{12} \\ & + 0.195C_6H_{12} + 0.089C_6H_{14} + 0.169C_7H_{14} + 0.072C_7H_{16} + 0.152C_8H_{16} \\ & + 0.012C_8H_{18} + 0.053C_9H_{18} + 0.003C_9H_{20} \end{aligned} \quad (1)$$

The reaction rate constant is given by Arrhenius expression:

$$K = k_0 \cdot \exp(-\frac{E_a}{RT}) \quad (2)$$

The variations in fluid properties depend mainly on the changes in the mass fraction and composition of the mixture caused by the pyrolysis reaction, as detailed description in Ref. [27].

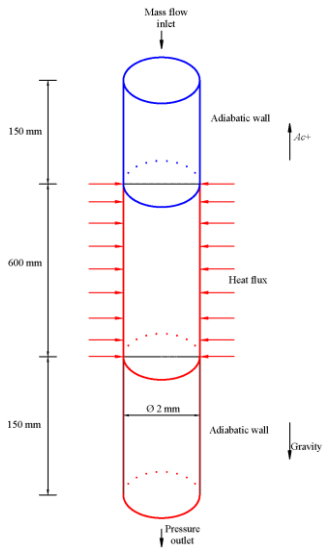

Figure 1. Schematic of the physical model.

2.3. Theoretical formulation and numerical treatment

The governing equations for mass, momentum, energy, and species mass fractions can be written as:

$$\nabla \cdot (\rho \vec{u}) = 0 \quad (3)$$

$$\nabla \cdot (\rho \vec{u}\vec{u}) = -\nabla p + \nabla \cdot \tau_{eff} + \rho g + \rho Ac \quad (4)$$

$$\nabla \cdot (\rho \vec{u} e_t) = \nabla \cdot (\lambda_{eff} \nabla T) - \nabla \cdot (p\vec{u}) + s_h \quad (5)$$

$$\nabla \cdot (\rho \vec{u} Y_j) = -\nabla \overrightarrow{J_j} + R_j \quad (6)$$

The turbulent flow was simulated in the k–ε model with enhanced wall treatment, which accurately predicted heat transfer in the tube. The k–ε turbulence equation is given by:

$$\nabla \cdot (\rho \vec{u} k) = \nabla \cdot ((\mu + \frac{\mu_t}{\sigma_k}) \nabla k) + G_k + G_b - \rho\varepsilon - Y_M \quad (7)$$

$$\nabla \cdot (\rho \vec{u} \varepsilon) = \nabla \cdot ((\mu + \frac{\mu_t}{\sigma_\varepsilon}) \nabla \varepsilon) + C_{1\varepsilon} \frac{\varepsilon}{k} (G_k + C_{3\varepsilon} G_b) - C_{2\varepsilon} \rho \frac{\varepsilon^2}{k} \quad (8)$$

These governing equations were solved using the SIMPLEC algorithm in the ANSYS Fluent 14.5 software. The appropriate convergence criteria for all equations were less than 10^{-6}, as detailed description in Ref. [27].

2.4. Grid independence verification

Grid independence verification is carried out using ICEM CFD software and ANSYS Fluent 14.5 software. As shown in Tab. 2, refining the mesh in the axial × radial directions from 900 × 40 to 1350 × 60 reduced the relative numerical errors in the wall temperature by less than 2%, whereas coarsening the mesh size from 900 × 40 to 600 × 27 increased the relative numerical errors to 3.9%. Therefore, the present numerical study was performed on the 900 × 40 (axial × radial) grid. Under the current computational conditions, the first near-wall node y^+ was kept at approximately 1.0, as required by the enhanced wall treatment.

Table 2. Grid specifications of computational domain (q = 1.2 MW/m^2, $\dot{m}$ = 5 g/s, T_{in} = 400 K and p = 5 MPa).

Case No	Number of elements (axial × radial)	Maximum relative error of T_w (%)
1	600× 27	3.9
2	900 × 40	2.0
3	1350 × 60	0

2.5. Model validation

The experimental conditions in Ref. [26] are stated as follows: p = 3.45 MPa, $T_w = f(x)$, T_{in} = 473 K, and u_o = 0.042 m/s. As shown in Fig. 2, the simulation results of T_f along the heated tube were consistent with the experimental results in Ref. [26].

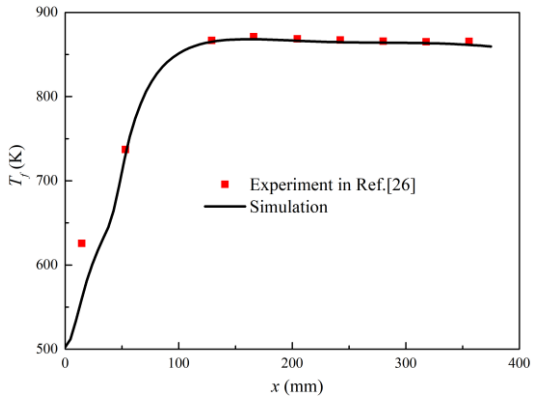

Figure 2. Comparisons of bulk fluid temperature distributions in our present simulations and the experimental data in Ref. [26].

The T_f and T_w along the heated tube were validated in a simulation case of n-decane, as described in Ref. [28]. The simulation conditions in Ref. [28] are stated as follows: p = 5 MPa, q_w = 1.2 MW/m^2, T_{in} = 400 K, and $\dot{m}$ = 2 g/s. As shown in Fig. 3, the relative errors of the predicted T_f and T_w were within ±3.2%. The simulation results well agreed with those in Ref. [28], confirming that the present simulation method is reliable and accurately predicts the supercritical heat transfer characteristics of n-decane at 5 MPa.

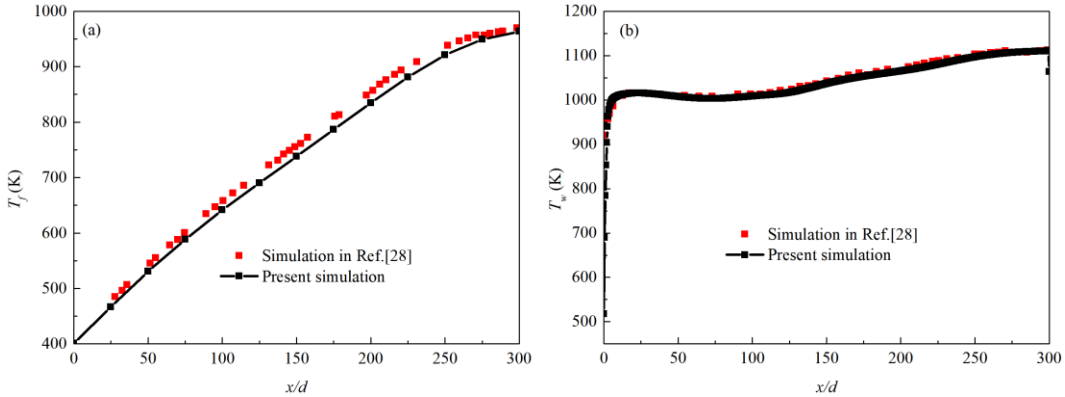

Figure 3. Comparisons of (a) bulk fluid temperature and (b) wall temperature distributions in our present simulations and the data simulated in Ref. [28].

3. Results and discussion

3.1. Effect of flow direction

Figure 4 presents distributions of wall temperatures (T_w) and convective heat transfer coefficients (h) in upward and downward flows. The local T_w was higher for the upward flow (Fig. 4a), because buoyancy accelerated the fluid near the wall for vertically upward flow, thus reducing velocity difference between the viscous layer and the core. The upward flow also produced a higher peak T_w than the downward flow. Meanwhile, the heat transfer was 9.1% higher in the vertical downward flow than in the vertical upward flow at x = 250 mm (Fig. 4b). The h was relatively low in the vertical upward flow, indicating that the HTD phenomenon more likely occurs in the vertical upward flow of supercritical n-decane.

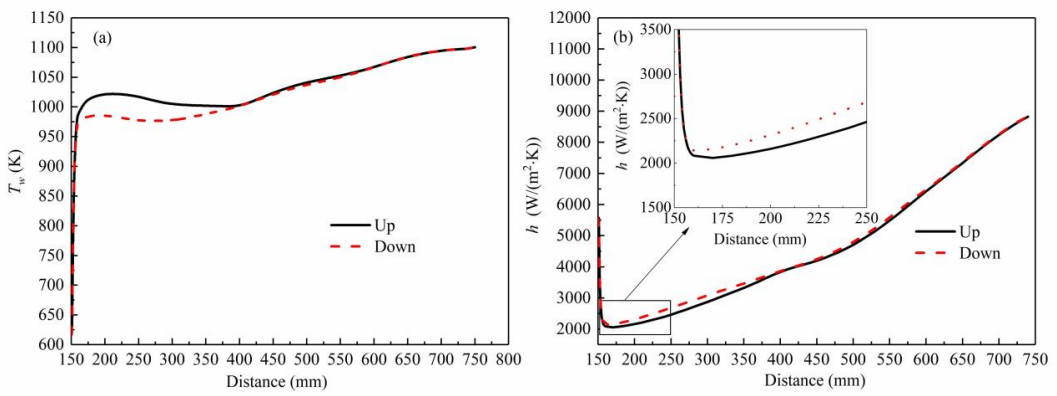

Figure 4. Distributions of (a) wall temperature and (b) convective heat transfer coefficient in different flow directions (q = 1.2 MW/m^2, T_{in} = 400 K, $\dot{m}$ = 2 g/s, g = 9.8 m/s^2, and p = 5 MPa).

3.2. Effects of mass flow rate

The HTD is directly reflected in the distributions of T_w and h on the heated wall. Figures 5a and 5b present the T_w and h distributions, respectively, along the tube length for different mass flow rates ($\dot{m}$ = 2, 3, 4, 5, and 6 g/s). The local Re in the vertical circular tube varied from 4358 to 65244 at $\dot{m}$ = 2 g/s. At x < 550 mm, increasing the $\dot{m}$ decreased the T_w and increased the h. This is because larger $\dot{m}$ leads to higher Re and stronger heat transfer performance. However, at x > 550 mm, h first decreased and then increased with increasing $\dot{m}$. As shown in Fig. 5b, h was greater at 2 g/s than at 3 g/s, mainly because the conversion of n-decane gradually decreased with increasing $\dot{m}$ (see Fig. 5d). At $\dot{m}$ = 2 g/s, the conversion was relatively high, and the chemical heat sink of the fuel dominated at the outlet section, thereby increasing the h. As $\dot{m}$ increased, the conversion gradually decreased while the influence of Re on h gradually increased. When $\dot{m}$ > 4 g/s, the influence of Re on h dominated; therefore, h became an increasing function of $\dot{m}$.

According to Urbano and Nasuti's theory [15], the HTD onset threshold can be taken as the q_w/G when minimum dT_w/dx = 0. Figure 5c shows effects of $\dot{m}$ on HTD onset. Decreasing $\dot{m}$ gradually reduced the minimum dT_w/dx, indicating that HTD more likely occurs at low $\dot{m}$. The HTD showed an increasingly delayed start point as $\dot{m}$ increased and disappeared at $\dot{m}$ = 6 g/s. Therefore, the HTD problem can be solved by increasing $\dot{m}$.

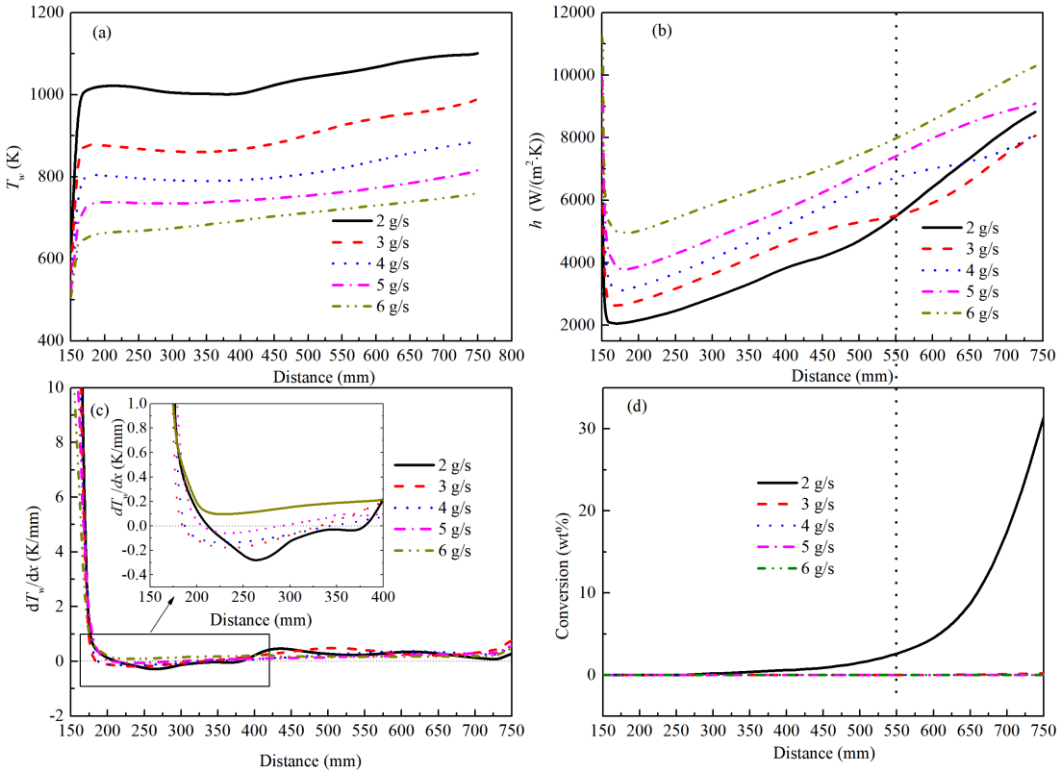

Figure 5. Distributions of (a) wall temperature, (b) convective heat transfer coefficient, (c) dT_w/dx, and (d) conversion at different mass flow rates (q = 1.2 MW/m^2, T_{in} = 400 K, g = 9.8 m/s^2, and p = 5 MPa). Inset in (c) enlarges the boxed region in the main graph.

3.3. Effects of heat flux

Figures 6a and 6b present the T_w and h distributions, respectively, under various heat fluxes at $\dot{m}$ = 2 g/s, T_{in} = 400 K, g = 9.8 m/s^2, and p = 5 MPa. T_w decreased with decreasing heat flux q. When q decreased to 0.4 MW/m^2, no obvious HTD was observed. At such low q, the temperature difference between the fluid and the tube wall was relatively small, and the buoyancy effect was too low to initiate the HTD. Therefore, the HTD problem can be solved by reducing q. As shown in Fig. 6b, the h first decreased and then increased with increasing distance.

Figure 6c shows the dT_w/dx distribution for various q at $\dot{m}$ = 2 g/s, T_{in} = 400 K, g = 9.8 m/s^2, and p = 5 MPa. Increasing q reduced the minimum value of dT_w/dx. The minimum dT_w/dx reached zero at q/G = 0.77 kJ/kg, implying that HTD will occur when $q/G > q_{onset}/G$ = 0.77 kJ/kg. Figure 6d shows the change trends of n-decane conversion for various q. Increasing q was found to increase the conversion and chemical heat sink. When q > 0.8 MW/m^2 and x > 550 mm, the cracking reaction of n-decane became obvious. As the cracking reaction is endothermic, a higher conversion implies that the chemical reaction absorbs more heat. Therefore, the slope of the h versus x curve increased with q (Fig. 6b).

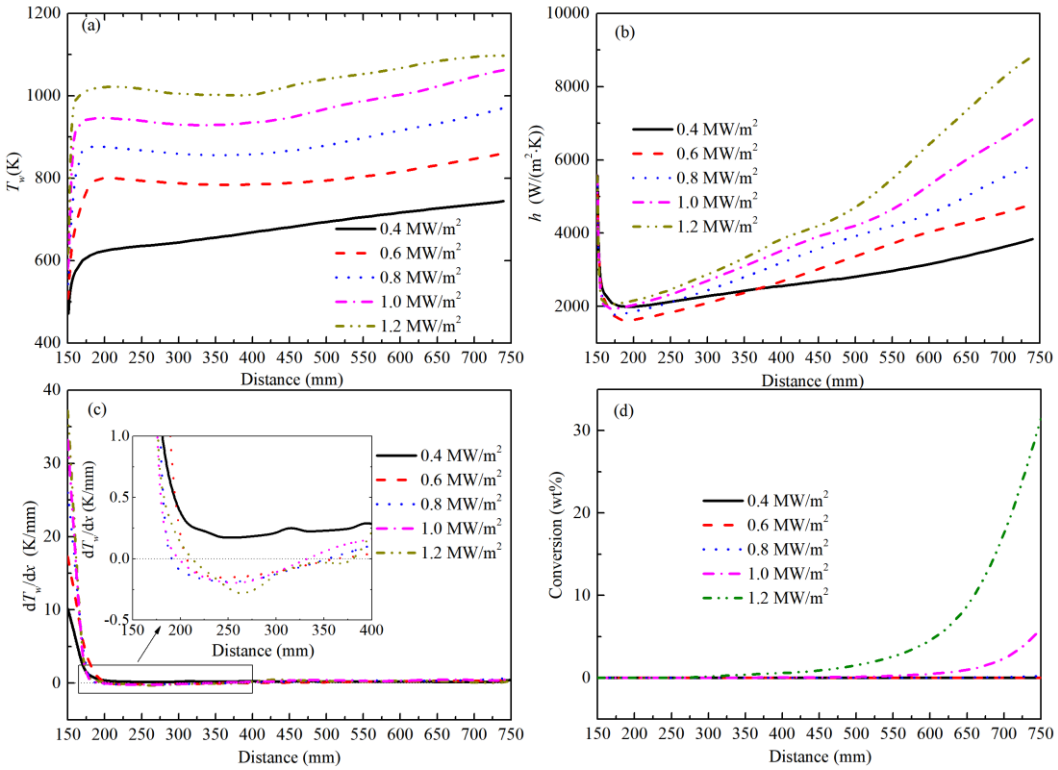

Figure 6. Distributions of (a) wall temperature, (b) convective heat transfer coefficient, (c) dT_w/dx, and (d) conversion at various heat fluxes ($\dot{m}$ = 2 g/s, T_{in} = 400 K, g = 9.8 m/s^2, and p = 5 MPa). Inset in (c) enlarges the region pointed by the arrow in the main graph.

3.4. Effect of inlet temperature

Distributions of T_w and h along the tube length were presented in Fig. 7a and 7b. The peak value of T_w decreased with increasing T_{in} (Fig. 7a). As T_{in} increased beyond 450 K, the HTD gradually disappeared, and no sharp rise appeared in T_w. Similar expressions were observed in Ref. [23]. In other words, the HTD was observed only within a certain range of T_{in} at fixed q/G (see Fig. 7c). Meanwhile, as T_{in} increased, the starting point of HTD moved forward, and the h gradually increased (Fig. 7b). The change trends of h were very similar at each T_{in}, showing a sharp decrease, followed by a gradual increase.

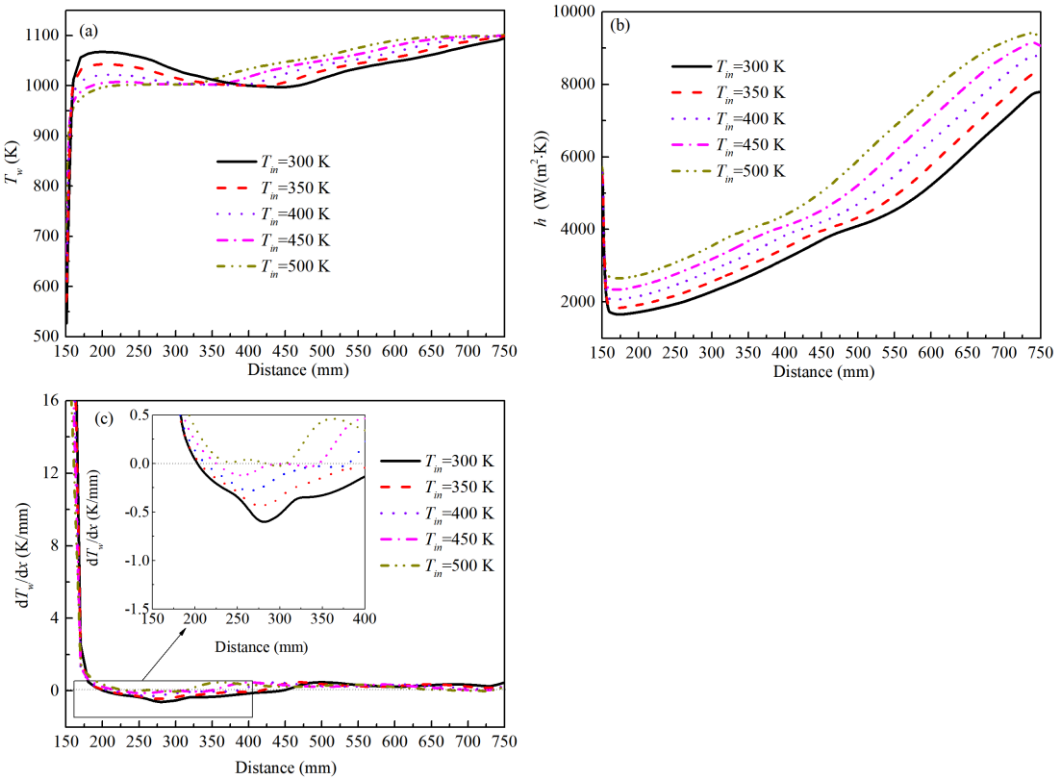

Figure 7. Distributions of (a) wall temperature, (b) convective heat transfer coefficient, and (c) dT_w/dx at different inlet temperatures ($\dot{m}$ = 2 g/s, q = 1.2 MW/m^2, g = 9.8 m/s^2, and p = 5 MPa). Inset in (c) enlarges the boxed region in the main graph.

3.5. Effects of flight acceleration

Figures 8a, 8b, and 8c present the T_w, h and dT_w/dx distributions, respectively, for different flight accelerations Ac. At q/G = 1.88 kJ/kg, the local T_w and h were slightly affected by the upward acceleration but were greatly affected by the upward deceleration. Between Ac = 0 and Ac = 29.4 m/s^2, the peak T_w differed by 77 K. The results show that the HTD becomes more serious as Ac increases under this condition. The peak T_w was the highest for upward deceleration, intermediate at zero acceleration, and the lowest for upward acceleration, indicating that the HTD caused by zero acceleration in the vertical upward flow will be relieved by imposing an upward acceleration. As shown in Fig. 8c, increasing the Ac of upward deceleration drove the minimum dT_w/dx to levels far below zero. When the Ac of upward deceleration reached 29.4 m/s^2, obvious HTD appeared.

Figure 9 shows the distributions of the fluid velocities in the vertical upward flow at Ac = −29.4, 0, and 29.4 m/s^2. When the Ac of the upward deceleration reached 29.4 m/s^2 (Fig. 9a), the flight acceleration and inertial force acted in opposite directions. Increasing both the Ac and buoyancy force increased the acceleration of the low-density fluid near the wall relative to the high-density fluid in the core flow. Therefore, the velocity of the near-wall fluid exceeded that of the core area in the 200–260 mm region, forming a typical M-shaped velocity distribution (Fig. 9a). When the flow was vertically accelerated, the Ac and inertial forces acted in the same direction (Figs. 9b and 9c). Increasing the Ac decreased the buoyancy; therefore, the low-density fluid near the wall was accelerated relatively slowly. In this scenario, the small space occupied by the high-speed fluid at a given position increased the mixing effect between the core and near-wall regions, thus enhancing the heat transfer of the fluid.

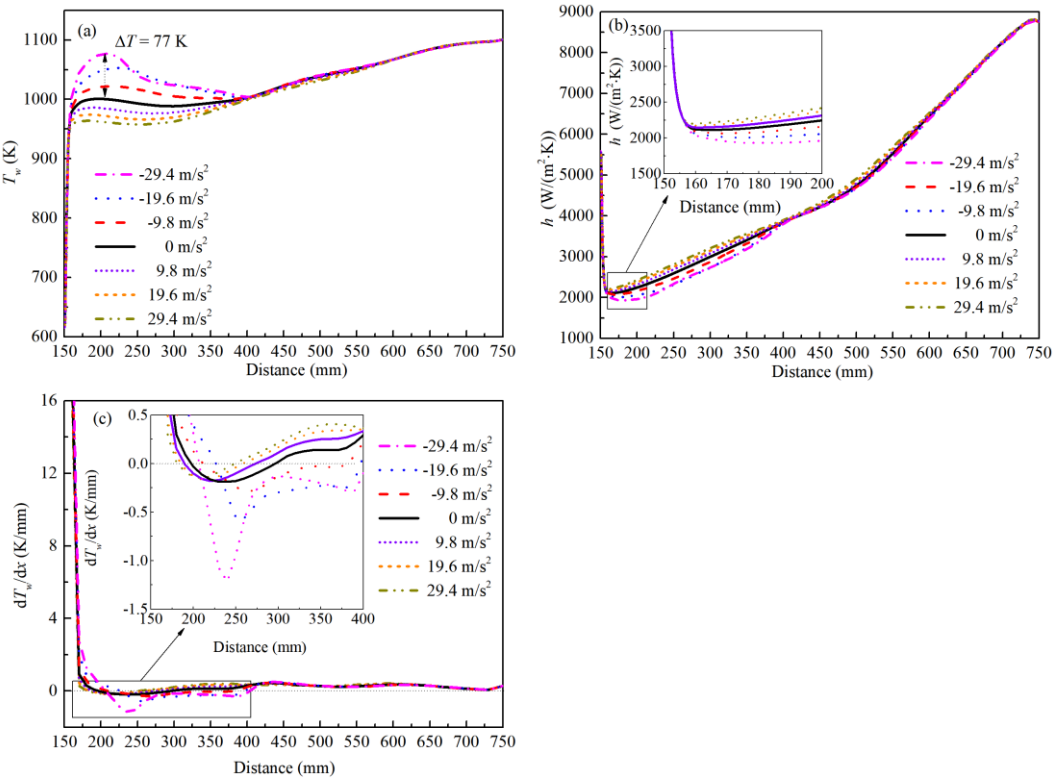

Figure 8. Distributions of (a) wall temperatures, (b) convective heat transfer coefficients, and (c) dT_w/dx for different flight accelerations ($\dot{m}$ = 2 g/s, q = 1.2 MW/m^2, T_{in} = 400 K, and p = 5 MPa).

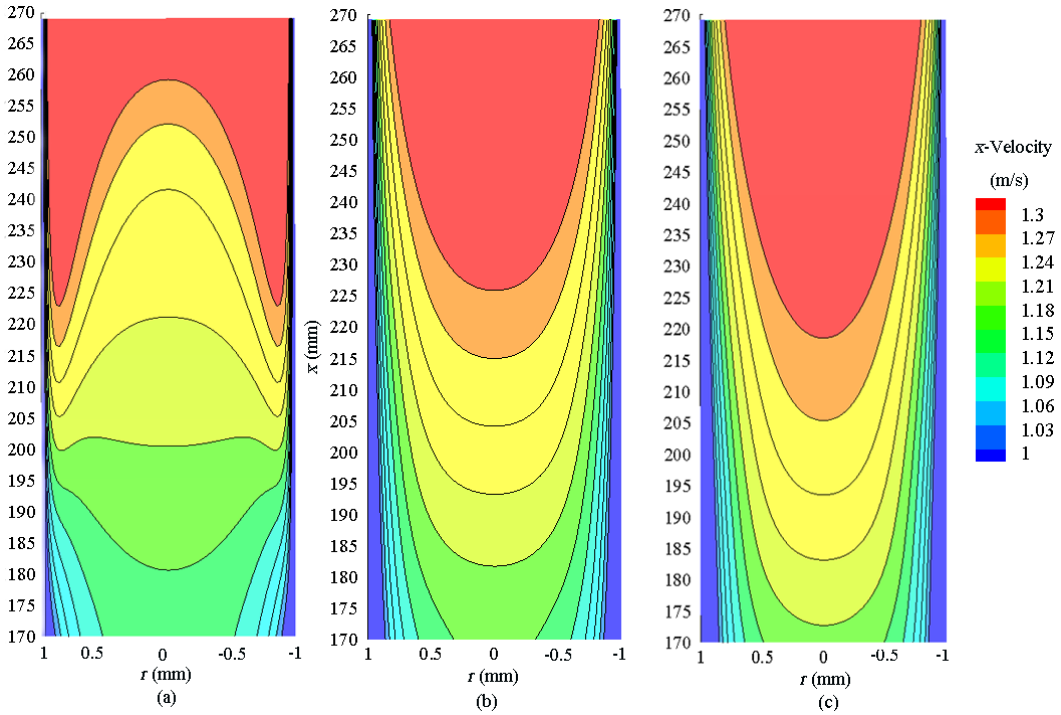

Figure 9. Distributions of fluid velocities with different flight accelerations in the vertical upward flow: (a) −29.4 m/s^2, (b) 0 m/s^2, and (c) 29.4 m/s^2 ($\dot{m}$ = 2 g/s, q = 1.2 MW/m^2, T_{in} = 400 K, and p = 5 MPa).

3.6. Prediction of the HTD

HTD is generally predicted using the critical heat flux correlation, which is established from the relationship between the heat and the mass fluxes. As discussed above, the HTD is gradually diminished by decreasing the heat flux q and increasing the mass flux $\dot{m}$, inlet temperature T_{in}, and acceleration Ac in the flow direction. Therefore, the HTD boundary must be established through the coupling effects of these four parameters. Figure 10 shows the HTD boundary at constant operating pressure (5 MPa) and varying mass flow rates (2–6 g/s), inlet temperatures (300–450 K), flight accelerations (−29.4–29.4 m/s^2), and heat fluxes (0.4–1.2 MW/m^2). The curved surface in Fig. 10 marks the boundary between HTD occurrence (above the surface) and HTD avoidance (below the surface). Therefore, the critical heat flux correlation based on $\dot{m}$, T_{in} and Ac is established by the curve fitting tool of MATLAB software from Fig. 10 as:

$$q_{onset} = \left(-0.4909 + 0.0032T_{in} + 0.0023Ac\right)G \tag{9}$$

The application range of this correlation is: p = 5 MPa, Ac = −29.4–29.4 m/s^2, T_{in} = 300–450 K, G = 2–6 g/s, and q = 0.4–1.2 MW/m^2. The R^2 value is 0.92. When q exceeds q_{onset} calculated by Eq. (9), HTD occurs.

In Ref. [6], when T_{in} = 340 K, Ac = 0, and p = 5 MPa, the corresponding critical conditions for the onset of HTD is (q/G) = 0.7 kJ/kg. According to Eq. (9) in this paper, under the above conditions, it can be calculated that (q/G) = 0.6 kJ/kg. Hence, a new correlation calculated by Eq. (9) is proposed to predict the critical heat flux for HTD of n-decane.

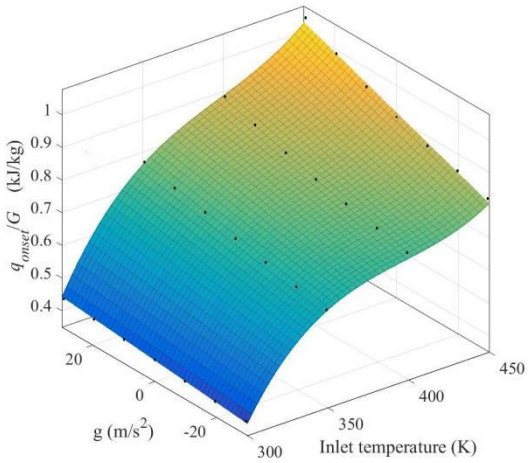

Figure 10. Distributions of boundary of heat transfer deterioration under the coupled effects of q, $\dot{m}$, T_{in}, and Ac.

4. Conclusions

In this paper, the influences of various factors (flow direction, mass flow rate, wall heat flux, inlet temperature, and flight acceleration) on thermal cracking and heat transfer characteristics of n-decane were studied in a vertical circular channel. The heat transfer characteristics were analyzed by plotting the variation trends of wall temperatures and heat transfer coefficients of n-decane. The conclusions can be drawn below:

(1) For the vertical upward flow, the convective heat transfer coefficient first decreased and then increased with the increased mass flow rate at x > 550 mm when q = 1.2 MW/m^2, T_{in} = 400 K, g = 9.8 m/s^2, and p = 5 MPa. The influences of mass flow rate depended mainly on absorption capacity of thermal energy and *Re*.

(2) The starting point of the HTD gradually moved forward as the buoyancy effect was attenuated. The HTD was diminished by increasing the inlet temperature and occurred only within a certain inlet temperature range at fixed q/G. A high upward deceleration induced the typical M-shaped velocity distribution of severe HTD, whereas the upward acceleration slightly affected the heat transfer.

(3) The critical heat flux relationship considering the flight acceleration and inlet temperature was established for the upward flow of vertical circular tube.

Acknowledgment

This work was financially supported by the Fundamental Research Funds for the Central Universities—Doctorate Innovation Capability Improvement Project (PHD2023-064), the Fundamental Research Funds for the Central Universities—Youth Fund Project (QJ2023-049).

Nomenclature

Ac	flight acceleration (ms^{-2})	Re	Reynolds number
c_p	specific heat at constant pressure (Jkg^{-1}K^{-1})	s_h	heat of chemical reaction (J)
$C_{1\varepsilon}$, $C_{2\varepsilon}$, $C_{3\varepsilon}$	constants in k-ε turbulence models	T	temperature (K)
e_t	total energy per unit mass (Jkg^{-1})	u	velocity (ms^{-1})
E_a	activation energy, 263.7 (kJmol^{-1})	$\vec{u}$	velocity vector (ms^{-1})
g	gravitational acceleration, 9.8 (ms^{-2})	x	x - axis coordinate (m)
G	mass flux (kgm^{-2}s^{-1})	y^+	dimensionless distances from the wall
G_k, G_b	production term	Y_j	mass fraction of species j (%)
h	heat transfer coefficient (Wm^{-2}K^{-1})	Y_M	contribution of the fluctuating dilatation
HTD	heat transfer deterioration	*Greek symbols*	
$\vec{J}_j$	diffusion flux of species j (m^{2}s^{-1})	ε	turbulent dissipation rate (m^{2}s^{-3})
k	turbulence kinetic energy (m^{2}s^{-2})	λ	thermal conductivity (Wm^{-1}K^{-1})
k_0	pre-exponential factor, 1.6×10^{15} (s^{-1})	μ	viscosity (kgm^{-1}s^{-1})
K	reaction rate (s^{-1})	ρ	density (kgm^{-3})
l	length of the tube (m)	σ_k, σ_ε	turbulent Prandtl number
$\dot{m}$	mass flow rate (gs^{-1})	τ	shear stress (Nm^{-2})
n	index	*Subscripts*	
Nu	Nusselt number	eff	effective value
p	pressure (MPa)	f	bulk fluid
Pr	Prandtl number	in	inlet
PPD	proportional product distribution	j	species
q	heat flux (kWm^{-2})	pc	pseudo critical
r	r - axis coordinate (m)	t	turbulent
R	universal gas constant, 8.314 × 10^{-3} (kJmol^{-1}K^{-1})	w	wall
R_j	net rate of production of species j (s^{-1})	onset	critical

References

[1] Chen, M., *et al*., Study on influence of forced vibration of cooling channel on flow and heat transfer of hydrocarbon fuel at supercritical pressure, *Thermal Science*, *26* (2022), 4 Part B, pp. 3463-3476.

[2] Kaur, I., P. Singh, Flow and thermal transport of supercritical n-decane in square minichannel featuring uniformly spaced tetrakaidecahedron-shaped unit cells, *International Communications in Heat and Mass Transfer*, *145* (2023), pp. 106835.

[3] Kline, N., *et al.*, Onset of heat transfer deterioration in vertical pipe flows of CO_2 at supercritical pressures, *International Journal of Heat and Mass Transfer*, *118* (2018), pp. 1056-1068.

[4] Liang, J., *et al.*, Flight acceleration effect on heat transfer deterioration of actively cooled scramjet engines, *Journal of Thermophysics and Heat Transfer*, *30* (2016), 2, pp. 279-287.

[5] Chang, F., *et al.*, Heat transfer deterioration and circumferential wall temperature inhomogeneity in a helically coiled tube carrying supercritical water: An intensive numerical simulation, *International Journal of Thermal Sciences*, *192* (2023), pp. 108386.

[6] Wang, Y., *et al.*, Numerical study on heat transfer deterioration of supercritical n-decane in horizontal circular tubes, *Energies*, *7* (2014), 11, pp. 7535-7554.

[7] Liu, Z., *et al.*, *Numerical analysis of heat transfer deterioration of China RP-3 aviation kerosene in a circular tube at supercritical pressures*, 11th AIAA/ASME Joint Thermophysics and Heat Transfer Conference, 2014, pp. 3358.

[8] Dang, G., *et al.*, Numerical study of heat transfer deterioration of turbulent supercritical kerosene flow in heated circular tube, *International Journal of Heat and Mass Transfer*, *85* (2015), pp. 1003-1011.

[9] Han, Y., *et al.*, Effect of vibration in cooling channel on heat transfer of aviation kerosene flowing under different pressures, *Thermal Science*, *27* (2023), 1 Part A, pp. 151-166.

[10] Xu, R. N., *et al.*, Buoyancy effects on turbulent heat transfer of supercritical CO_2 in a vertical mini-tube based on continuous wall temperature measurements, *International Journal of Heat and Mass Transfer*, *110* (2017), pp. 576-586.

[11] Sun, X., *et al.*, Buoyancy effects on supercritical-pressure conjugate heat transfer of aviation kerosene in horizontal tubes, *The Journal of Supercritical Fluids*, *139* (2018), pp. 105-113.

[12] Petukhov, B., *et al.*, Turbulent flow and heat transfer in horizontal tubes with substantial influence of thermos-gravitational forces, *Proceeding of Fifth International Heat Transfer Conference*, Tokyo, Japan, 1974.

[13] Li, Y., *et al.*, Heat transfer deterioration in upward and downward pipe flows of supercritical n-decane for actively regenerative cooling, *International Journal of Thermal Sciences*, *168* (2021), 3, pp. 107066.

[14] Zhang, Q., *et al.*, Study on identification method of heat transfer deterioration of supercritical fluids in vertically heated tubes, *International Journal of Heat and Mass Transfer*, *127* (2018), pp. 674-686.

[15] Urbano, A., F. Nasuti, Onset of heat transfer deterioration in supercritical methane flow channels, *Journal of Thermophysics and Heat Transfer*, *27* (2013), 2, pp. 298-308.

[16] Koshizuka, S., *et al.*, Numerical analysis of deterioration phenomena in heat transfer to supercritical water, *International Journal of Heat and Mass Transfer*, *38* (1995), 16, pp. 3077-3084.

[17] Huang, D., W. Li, Heat transfer deterioration of aviation kerosene flowing in mini tubes at supercritical pressures, *International Journal of Heat and Mass Transfer*, *111* (2017), pp. 266-278.
[18] Yamagata, K., *et al.*, Forced convective heat transfer to supercritical water flowing in tubes, *International Journal of Heat and Mass Transfer*, *15* (1972), 12, pp. 2575-2593.
[19] Mokry, S., *et al.*, Development of supercritical water heat-transfer correlation for vertical bare tubes, *Nuclear Engineering and Design*, *241* (2011), 4, pp. 1126-1136.
[20] Zhou, W., *et al.*, Deterioration in heat transfer of endothermal hydrocarbon fuel, *Journal of Thermal Science*, *20* (2011), 2, pp. 173-180.
[21] Xie, J., *et al.*, A review of heat transfer deterioration of supercritical carbon dioxide flowing in vertical tubes: Heat transfer behaviors, identification methods, critical heat fluxes, and heat transfer correlations, *International Journal of Heat and Mass Transfer*, *149* (2020), pp. 119233.
[22] Schatte, G. A., *et al.*, Development of a new empirical correlation for the prediction of the onset of the deterioration of heat transfer to supercritical water in vertical tubes, *International Journal of Heat and Mass Transfer*, *113* (2017), pp. 1333-1341.
[23] Guo, J., *et al.*, Thermal-hydraulic characteristics of supercritical pressure CO_2 in vertical tubes under cooling and heating conditions, *Energy*, *170* (2019), pp. 1067-1081.
[24] Lv, L., *et al.*, Numerical investigation on convective heat transfer of supercritical aviation kerosene in a horizontal tube under hyper gravity conditions, *Aerospace Science and Technology*, *105* (2020), pp. 105962.
[25] Chen, Y., *et al.*, Influences of accelerating states on supercritical n-decane heat transfer in a horizontal tube applied for scramjet engine cooling, *Aerospace Science and Technology*, *109* (2021), pp. 106424.
[26] Ward, T., *et al.*, Simulations of flowing mildly-cracked normal alkanes incorporating proportional product distributions, *Journal of Propulsion and Power*, *20* (2004), 3, pp. 394-402.
[27] Lei, Z., *et al.*, Numerical study on supercritical heat transfer of n-decane during pyrolysis in rectangular tubes, *Applied Thermal Engineering*, *170* (2020), pp. 115002.
[28] Tao, Z., *et al.*, Numerical investigation of pyrolysis effects on heat transfer characteristics and flow resistance of n-decane under supercritical pressure, *Chinese Journal of Aeronautics*, *31* (2018), 6, pp. 1249-1257.

Submitted: 08.12.2023.
Revised: 05.06.2024.
Accepted: 10.06.2024.